Lasers in Manufacturing Conference 2023

# Laser interference-treatment tunes surface states and corrosion behavior of additively manufactured near-beta Ti alloy

Frederic Schell[a,*], Phil Goldberg[b], Avinash Hariharan[b], Martin Hantusch[b], Magdalena Ola Cichocka[b], Nicolás Pérez[b], Andrea Voß[b], Lars Giebeler[b], Volker Hoffmann[b], Christoph Zwahr[a], Andrés Fabián Lasagni[a,c], Annett Gebert[b]

[a]*Fraunhofer Institute for Material and Beam Technology IWS, Winterbergstr. 28, 01277 Dresden, Germany*
[b]*Leibniz Institute for Solid State and Materials Research (IFW) Dresden, Helmholtzstr. 20, 01069 Dresden, Germany*
[c]*Institut für Fertigungstechnik, Technische Universität Dresden, Georg-Bähr-Str. 3c, 01069 Dresden, Germany*

**Abstract**

Near-beta titanium alloys are promising bone implant materials due to their low elastic modulus and good corrosion resistance. To optimize their surface properties, we apply direct laser interference patterning (DLIP) microtextures using nano (ns)- and picosecond (ps) pulses to an additively manufactured Ti-13Nb-13Zr alloy. It was observed that both the surface topography and chemistry as well as the microstructure are affected by the laser treatment. Single- and multiscale topographies were obtained by ns- and ps-DLIP, respectively. The nanosecond texturing led to an increased cubic β-phase fraction and the formation of a 25 nm thick passive layer, resulting in improved corrosion resistance. The ps-DLIP exhibited a defective surface oxide layer and a larger surface area due to the multi-scale topography, but nonetheless achieved improved corrosion resistance related to a partial wetting state.

Keywords: laser powder bed fusion; direct laser interference patterning; beta titanium alloy; corrosion

## 1. Introduction

In recent years, there has been an increasing demand for biocompatible materials for use as implantable medical devices. Titanium and its alloys are widely used for this purpose due to their excellent mechanical properties, good biocompatibility, and corrosion resistance. Near-beta titanium alloys, in particular, have been shown to be promising for biomedical application as bone implants due to their low elastic modulus and excellent corrosion resistance. Recently, Hariharan et al., 2022 showed how additive manufacturing techniques and heat treatment could be used to fabricate biocompatible implants made of Ti-13Nb-13Zr and

to tailor the alloy microstructure for further improvement in mechanical properties (e.g. reduction in elastic modulus). However, there is still a potential for improvement in terms of surface properties to enhance the implant biofunctionality for an improved biological cell response. One promising approach is to apply Direct Laser Interference Patterning (DLIP) to fabricate periodic microtextures on the surface within a laser pulse and at high throughput. This technique allows for precise control over the surface topography while also influencing the surface chemistry, which can in turn affect the microstructure and properties of the surface material. Previous studies on DLIP-treated titanium alloys by Zwahr et al., 2019 have shown beneficial effect of picosecond surface textures on cell viability. Kuczyńska-Zemła et al., 2021 observed improved corrosion resistance of nanosecond-DLIP textured titanium in a physiological saline solution at 37°C that simulates the human body environment. However, existing studies of DLIP patterning of titanium are usually focused on classically manufactured pure titanium. Moreover, a direct comparison between the effects of nanosecond and picosecond pulsed DLIP has not yet been drawn. In our previous studies, we investigated the effect of different pulse durations on the surface topography of Ti-13Nb-13Zr, as shown in Schell et al., 2022, where single-scale DLIP topographies were obtained for ns-DLIP and multi-scale topographies were obtained for ps-DLIP.

In this present study, we apply DLIP microtextures using both nano- and picosecond pulses to the near-beta Ti-13Nb-13Zr alloy that was fabricated using laser powder bed fusion (LBPF). We investigate the effect of the laser treatment on the surface topography, chemistry, and microstructure, as well as the resulting corrosion resistance. Our findings demonstrate the potential of DLIP microtexturing as a method for improving the surface properties of near-beta titanium alloys for use as implantable medical devices. The results here presented summarize the findings already published by Goldberg et al., 2023.

## 2. Materials and Methods

### *2.1. Materials and texturing*

All experiments were conducted on near-beta Ti-13Nb-13Zr alloy samples fabricated via LPBF process. Rods of 12 mm diameter were wirecut into 2 mm thick discs that were then ground with SiC abrasive paper to achieve a surface rouchness (Sa) of 0.2 µm. The properties of the specimens were analyzed in detail in Hariharan et al., 2022.

Ti-13Nb-13Zr discs were textured using a two-beam DLIP configuration consisting of a diffractive optical element to split the main beam into two subbeams. The beams are parallelized by a prism and brought to interfere on the substrate surface under a specific angle that depends on the distance between the diffractive optical element and the prism. The overlapping beams produce a line-like interference pattern on the substrate surface with a spatial period that depends on the laser wavelength and the angle between the beams. The DLIP optical assembly is used in conjunction with both a nanosecond-pulsed (Laser Export, TECH-1053, Basic) and picosecond-pulsed (Edgewave, PX-200) diode-pumped solid-state laser. A more detailed description of the fabrication process can be found in Schell et al., 2022.

Table 1. Properties of the laser sources utilized for DLIP texturing of Ti-13Nb-13Zr specimens.

| Laser | Pulse duration | Wavelength (nm) | Max. pulse energy (µJ) | $M^2$ | Mode | Interference diameter (µm) |
|---|---|---|---|---|---|---|
| Nanosecond | 6 ns | 1053 | 500 | < 1.3 | $TEM_{00}$ | 120 |
| Picosecond | 10 ps | 1064 | 800 | < 1.3 | $TEM_{00}$ | 210 |

*2.2. Topography characterization*

The surface roughness and 3D topography representation of the samples were obtained using a confocal laser-scanning microscope (CLSM) with a 404 nm laser and 150x magnification objective (Keyence, VK-X260). Additionally, higher resolution measurements were performed using an atomic force microscope (AFM, Bruker, Dimension Icon). A rectangular-shaped Si-cantilever (Olympus, OMCL-AC160TS) with a spring constant value of 26 N/m was used. A sharpened tetrahedral probe tip of 14 µm height and with 7 nm tip radius was positioned at the cantilever free triangular end. The cantilever was driven at 341 kHz resonance frequency. The AFM scanning over the sample surface was operated in tapping mode at a rate of 0.2 Hz. Surface topography inspection was carried out using a scanning electron microscope (SEM, JOEL, JSM 6610LV) at 15 kV accelerating voltage.

*2.3. GIXRD measurements*

Grazing incident X-ray diffraction (GIXRD) measurements with a 2° angle of incidence were conducted on a X'Pert3 Pro MRD diffractometer (Malvern Panalytical, Philips) with PW3050 goniometer and Cu-K$\alpha_1$ radiation ($\lambda$=1.540598 Å) in reflection mode. 2$\theta$ scans were carried out between 20° to 100° at 0.02° interval steps. To index the phase and estimate the phase fractions, the software "Panalytical HighScore Plus" and an ICDD PDF-4+ database (International Centre for Diffraction Data, Newtown Square, PA, USA) were used.

*2.4. Corrosion measurements*

DLIP-treated and untreated Ti-13Nb-13Zr discs were used as working and reference electrodes in electrochemical corrosion studies. Working electrodes were mounted in a plastic tube holder, electrically contacted at their rear side, and sealed with a water-insoluble polymer coating to inhibit crevice corrosion. Before each corrosion test, working electrode surfaces of reference specimens were ground with SiC 1200- and 2500-grade paper and stored in air for 20 hours to naturally passivate the surface. Electrochemical measurements were conducted in a phosphate-buffered saline solution at 37±1 °C using a three-electrode arrangement and a Solartron SI 1287 Electrochemical Interface. Open circuit potential measurements were followed by potentiodynamic polarization measurements, and results were plotted as current density versus applied potential. A minimum of five corrosion tests were performed for each surface state. The arithmetic mean values and standard deviations were determined from the measurement data.

**3. Results and discussion**

The two-beam DLIP treatment of the Ti-13Nb-13Zr samples with an interference angle of 6.1° resulted in line-like textures with a theoretical spatial period of 4.95 µm and 5.00 µm for the nanosecond- and picosecond-laser, respectively. SEM and CLSM shown in Figure 1 reveal the similar dominant periodic pattern with a measured period of 5.00 µm for ns-DLIP and 4.97 µm for ps-DLIP using 2D-FFT on the CLSM-measured files. The ns-DLIP topography is single-scaled and smooth, which is related to melting effects during the laser texturing.

The ps-DLIP topography however is characterized by superimposed laser-induced periodic surface structures (LIPSS) in the form of low spatial frequency LIPSS (LSFL) with a period of approximately 700 nm and high spatial frequency LIPSS (LSFL) with a period of approximately 200 nm. Using AFM measurements, the surface area of the textures was estimated by computing the developed interfacial area ratio Sdr, which represents the relative increase in surface area compared to the projected surface area, as published in

Goldberg et al., 2023. While the untextured reference sample had an Sdr value of 11 %, ns-DLIP texture achieves a 31% increase in surface area compared to an ideally flat sample. On the other hand, the ps-DLIP textured samples reach an Sdr of 372 %, which was attributed mostly to the contribution of the LSFL and HSFL nanoroughness. Consequently, the water contact angle of the textures differs signficiantly, as published in Goldberg et al., 2023. Due to the larger surface roughness and surface area of the ps-DLIP texture, a contact angle of approximately 160 ° is reached after 33 days, rendering the surface superhydrophobic. On the other hand, the ns-DLIP texture exhibits a contact angle 116 °, only reaching the moderately hydrophobic regime.

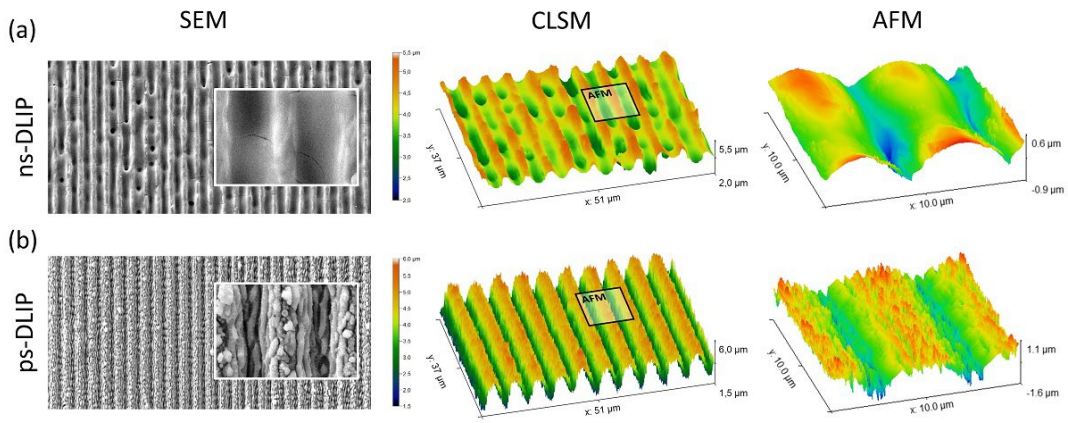


Fig. 1. SEM, CLSM and AFM measurements of the topography of (a) ns-DLIP and (b) ps-DLIP textured specimens with a spatial period of 5 µm and a peak-to-valley depth in the range of 1-2 µm. The ns-DLIP texture features single-scale channels with a smooth surface as a consequence of melting, whereas the ps-DLIP texture exhibits a multi-scale nanoroughness in the form of LSFL and HSFL on top of the DLIP channels. Adapted from Goldberg et al., 2023.

Crystallographic measurements were conducted using GIXRD (shown in Figure 2) and revealed that the untextured reference samples exhibited mostly the hexagonally packed α phase and the martensitic α′ phase as well as the orthorombic martensitic α′′ phase, which are typical for LBPF-produced Ti-13Nb-13Zr alloy. Although a slight amount of body-centered cubic β phase is expected to be observed after the LBPF process, it was not clearly detected in the measurement due to the angular overlapping with reflections from the dominant phases. Noteably, the ps-DLIP textured specimens show similar diffraction patterns as the untextured reference with a mixed microstructure containing α, α′ and α′′,. An additional peak at 32° was determined to correspond to an oxide phase with the nominal stoichiometry $Ti_{1.67}O_3$ and the orthorhombic structure. On the other hand, the ns-DLIP textured surfaces were characterized by a dominant β phase, with significantly less intensity in the peaks corresponding to α, α′ and α′′ phases.

This can be explained by the difference in the laser-material interaction between ns- and ps-DLIP as a result of the different pulse durations. Thermal simulations using the finite element method (FEM) were performed to estimate the temperature distrubution in the material surface during the irradiation with a two-beam interference pattern, as already published by Lasagni et al., 2009. The model was based on the heat diffusion equation and considers the heat required to melt and vaporize the material (latent heat). The simulation was simplified by using the thermal properties of pure titanium as given by Ready, 2021, and serves as an orientation to understand the differences in the processes. Figure 3 shows the simulated distributions of the solid, liquid and vapor phases during a single pulse with using ns-DLIP (a) and ps-DLIP (b) conditions.

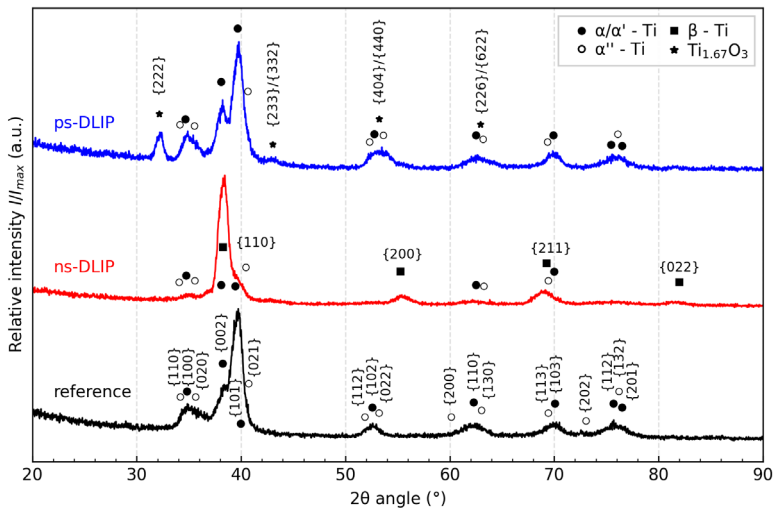


Fig. 2. GIXRD pattern of the untreaded (black), ns-DLIP textured (blue) and ps-DLIP textured (orange) Ti-13NB-13Zr specimens. Adapted from Goldberg et al., 2023.

In the case of ns-DLIP, a large amount of material is in the molten phase, penetrating up to ~450 nm into the material. In the center of the interference maxima, the material is vaporized up to a depth of approximately 350 nm. The resolidification time lies around ~200 ns. On the other hand, a single ps-DLIP pulse results in significantly more shallow structures with only a small amount of molten phase and a resolidification time < 1 ns due to negligible heat conduction as a result of the shorter pulse duration.

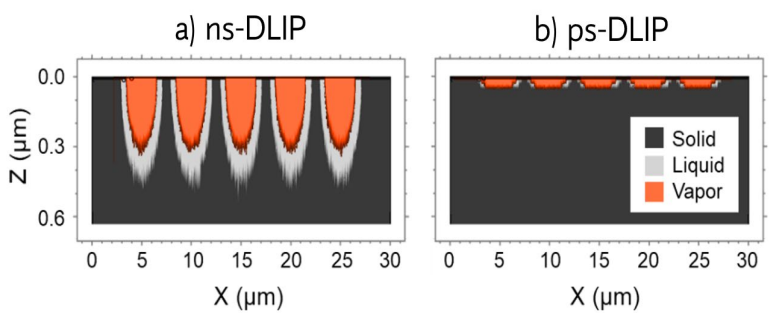


Fig. 3. Simulated regions of solid (dark grey), liquid (light grey) and vapor (red) phase under irradiation with a) ns-DLIP with 6 ns pulse duration and b) ps-DLIP with 10 ps pulse duration and an interference period of 5 µm under simplified conditions.

The corrosion resistance of the ns- and ps-DLIP textured specimen in PBS solution was compared to the untextured reference using potentiodynamic polarization measurements. The OCP measurements were performed and reached steady-state conditions after 2 h, showing approximately 200 mV higher positive OCP values for the DLIP-treated surfaces compared to the untextured LBPF reference (see Table 2), which is related to the increased surface oxidation due to the DLIP process, as elucidated in Goldberg et al., 2023. The larger OCP values indicate improved corrosion resistance. In the following, potentiodynamic measurements were

conducted versus the reference electrode referring to the saturated calomel electrode (SCE) potential, as shown in Figure 4. The current density values were scaled with the geometric (projected) surface areas of the samples. The potential at the minimum current density is defined as the corrosion potential $E_{Corr}$, which closely matches the OCP potential $E_{OCP}$ for all three surface states (reference, ns-DLIP, ps-DLIP), as given in Table 2.

Table 2. Corrosion parameters obtained from OCP measurements and polarization curves of the textured and untextured Ti-13Nb-13Zr surfaces (values taken from Goldberg et al., 2023).

| Surface | $E_{OCP}$ (V vs SCE) | $E_{Corr}$ (V vs SCE) | $I_{Corr}$ (nA/cm²) | $I_{pass}$ (µA/cm²) |
|---|---|---|---|---|
| reference | -0.334 ± 0.017 | -0.348 ± 0.016 | 51 ± 22 | 2.81 ± 0.11 |
| ns-DLIP | -0.132 ± 0.051 | -0.164 ± 0.059 | 30 ± 15 | 2.64 ± 0.24 |
| ps-DLIP | -0.128 ± 0.029 | -0.178 ± 0.045 | 68 ± 45 | 5.05 ± 0.40 |

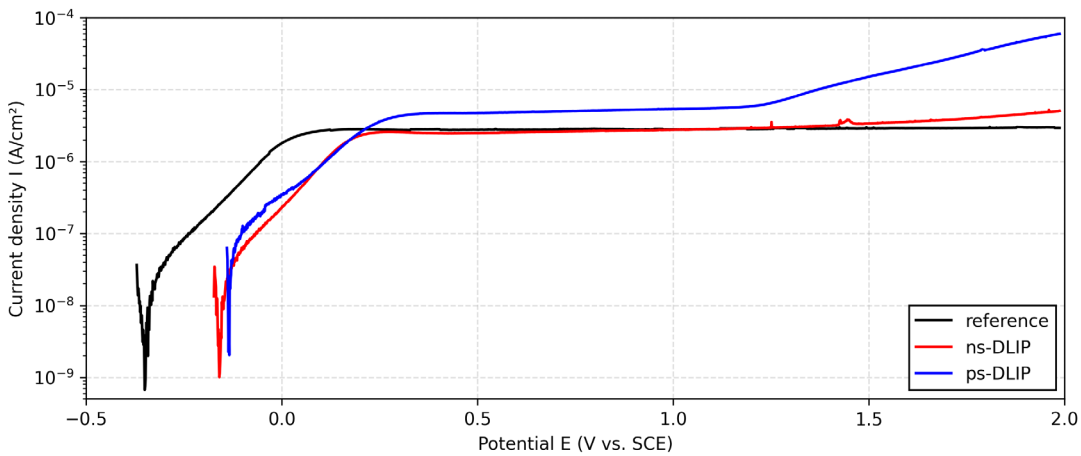


Fig. 4. Polarization curves of anodic current density potential curves for untreated (black), ns-DLIP textured (blue) and ps-DLIP textured (orange) Ti-13Nb-13Zr specimens in PBS solution at a typical human body temperature of 37 °C. Adapted from Goldberg et al., 2023.

Moreover, low extrapolated corrosion current densities $I_{Corr}$ imply low rates of free corrosion. Following a further increase of the external anodic potential, the current densities initially increase during the first 400 mV potential increase for all surfaces, before reaching a stabilized state called the passivation regime where the current density remains constant. The regime of increasing current densities is associated with the formation of a passive anodic state that replaces the initial passive oxide layer. However, with the external potential exceeding 1.2 V vs. SCE, the current densities of the ps-DLIP sample increase significantly, while the reference and ns-DLIP state continue to exhibit strong passivity. The observed effect in the case of ps-DLIP can be attributed to enhanced electron transfer for the water decomposition reaction due to the weak barrier effect of the defective oxide layer, as assumed by Goldberg et al., 2023. Nonetheless, the ps-DLIP state features a good corrosion resistance, which might be considered counter-intuitive when taking into account the significantly larger surface area. However, it is likely that the superhydrophobic surface properties resulted in a partial wetting state that inhibited the corrosion despite the increased surface area and defective oxide layer.

## 4. Conclusions

In this work, nanosecond and picosecond DLIP were applied to additively manufactured biocompatible Ti-13Nb-13Zr samples to form single-scale and multi-scale line-like microtextures on the surface. Using GIXRD measurements, it was shown that the ns-DLIP process induced a phase transformation, resulting in significantly increased presence of cubic β phase in the near-surface regions, whereas ps-DLIP had a similar microtextural composition as the untextured reference, which was characterized by the hexagonal α, the martensitic α′ and α′′ phases. The increased β phase fraction on ns-DLIP specimens was explained by the differences in laser-material interaction due to the longer pulse duration. OCP and potentiodynamic corrosion measurements were performed, which observed enhanced corrosion resistance on both types of textured surfaces. In the case of ns-DLIP, this was attributed to the enhanced passivation layer, while in the case of ps-DLIP the strong hydrophobicity and consequently the partial wetting state could explain the improved corrosion resistance despite the strongly increased surface area.

## Acknowledgements

This work was carried out in the framework of the OsteoLas project, partially financed by the European Regional Development Fund (EFRE) and by tax revenues on the basis of the budget adopted by the Members of the Parliament of Saxony (funding reference 100382988 / 100382989).

## References

Goldberg, P., Hariharan, A., Schell, F., Hantusch, M., Cichocka, M. O., Pérez, N., Voß, A., Giebeler, L., Hoffmann, V., Zwahr, C., Lasagni, A. F., Gebert, A., 2023. Fine-tuning effect of Direct Laser Interference Patterning on the surface states and corrosion behevior of a biomedical additively manufactured beta Ti alloy. Corrosion Science 219, p. 111230.

Hariharan, A., Goldberg, P., Gustmann, T., Maawad, E., Pilz, S., Schell, F., Kunze, T., Zwahr, C., Gebert, A., 2022. Designing the microstructural constituents of an additively manufactured near β Ti alloy for an enhanced mechanical and corrosion response. Materials & Design 217, p. 110618.

Kuczyńska-Zemła, D., Sotniczuk, A., Pisarek, M., Chlanda, A., Garbacz, H., 2021. Corrosion behavior of titanium modified by direct laser interference lithography, Surface and Coatings Technology, 418, p. 127219.

Lasagni, A., and Mücklich, F., 2009, FEM Simulation of Periodical Local Heating Caused by Laser Interference Metallurgy, Journal of Materials Processing Technology., 209 (1), pp. 202–209.

Ready, J. F., ed., 2021, LIA Handbook of Laser Materials Processing, Laser Institute of America/Magnolia, Springer, Berlin.

Schell, F., Hariharan, A., Goldberg, P., Baumann, R., Jäger, E., Gebert, A., Zwahr, C., Lasagni, A. F., 2022. Pulse duration and wavelength effects on the surface topography of Direct Laser Interference Patterning treated titanium specimen. Journal of Laser Micro/Nanoengineering 17, p. 199.

Zwahr, C., Welle, A., Weingärtner, T., Heinemann, C., Kruppke, B., Gulow, N. große Holthaus, M., Lasagni, A. F., 2019. Ultrashort Pulsed Laser Surface Patterning of Titanium to Improve Osseointegration of Dental Implants, Advanced Engineering Materials, 21, p. 1900639.